

Radiation-Induced Grain Growth of Nanocrystalline $\text{Al}_x\text{CoCrFeNi}$ High-Entropy Alloys

Jianren Zhou,* Md Imdadul Islam, Shengmin Guo, Yi Zhang, and Fengyuan Lu



Cite This: *J. Phys. Chem. C* 2021, 125, 3509–3516



Read Online

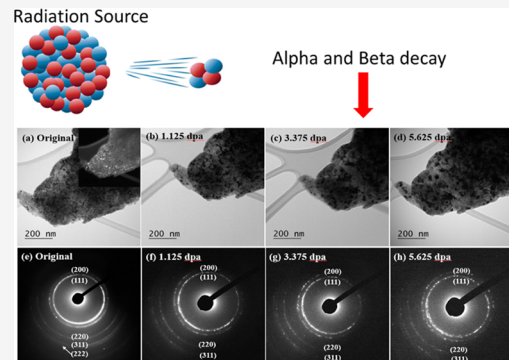
ACCESS |

Metrics & More

Article Recommendations

Supporting Information

ABSTRACT: Grain growth of nanocrystalline $\text{Al}_x\text{CoCrFeNi}$ high-entropy alloys with varying Al contents ($x = 0, 1, 2$) is studied. The alloys are fabricated by high-energy ball milling and subjected to a 1 MeV Kr^{2+} ion irradiation bombardment at room temperature up to a dose of 5.625 displacements per atom (dpa). X-ray diffraction (XRD) and transmission electron microscopy (TEM) characterizations show that the crystal structure is face-centered cubic (FCC) for CoCrFeNi (Al-0) alloy and BCC + FCC for $\text{Al}_1\text{CoCrFeNi}$ (Al-1) and $\text{Al}_2\text{CoCrFeNi}$ (Al-2) alloys. *In situ* TEM observations show that the grain size increases with irradiation dose from 13.8 ± 3 , 7.4 ± 1 , and 11 ± 1 nm before irradiation to 36 ± 8 , 25 ± 5 , and 26.6 ± 3 at 5.625 dpa for Al-0, Al-1, and Al-2 alloys, respectively, and a significant chemical composition dependence on grain growth was seen, where the highest grain growth rate is observed for the Al-2 alloy as a result of the lowest cohesive energy, which results in the lowest activation energy for atomic jump under ion irradiation. The grain growth kinetics is elucidated by the thermal spike model, and its mechanism is attributed to a disorder-driven mechanism for the initial fast growth, which is caused by the loss of the crystalline order as a result of ion-irradiation-induced large lateral damage volume and a defect-driven mechanism for the later slow growth stage, which is driven by the defect concentration difference near grain boundaries (GBs) under ion irradiation. Finally, this paper shows the effect of atomic collision cascades on grain growth, demonstrating the possibility to control grain sizes using the ion beam technique for nanostructured materials in nuclear applications.



1. INTRODUCTION

High-entropy alloys (HEAs) are composed of four or more metallic elements mixed in an equimolar or near-equimolar ratio to form a solid solution.^{1,2} HEAs exhibit good properties, including high elevated-temperature strength,^{3,4} low-temperature toughness,⁵ excellent wear,^{6,7} as well as corrosion^{8,9} and oxidation resistance,¹⁰ which showed the possibility of being structural materials^{11–16} for nuclear reactors. However, to be nuclear materials, a fundamental requirement is to endure high irradiation dose.^{17–21} The mixing of elements results in the possibility of achieving an extremely high irradiation resistance via unique damage-healing mechanisms,^{22–26} compared to a large number of crystal defects in traditional materials²⁷ in the radiation condition. In addition, the lack of bubbles and the resistance to void swelling make the HEAs show significant promise as nuclear structural materials. Some studies^{28–31} on HEAs showed them to be durable material candidates under extreme radiation conditions. For example, Zr-Hf-Nb²⁹ demonstrated an irradiation resistance up to a dose of 10 dpa and CoCrCuFeNi HEA³⁰ can hold an irradiation dose up to 40 dpa. Moreover, voids were not observed for FeNiMnCr HEA³² although the irradiation dose reached up to 10 dpa, and a lower volume swelling of $\text{Al}_x\text{CoCrFeNi}$ HEAs¹⁹ was revealed compared to conventional structural materials under similar irradiation conditions. These encouraging results make HEAs

very attractive for use as nuclear materials. Therefore, it is of great importance to developing new HEAs with good irradiation performances to meet the enhanced requirements for advanced nuclear reactors.

The $\text{Al}_x\text{CoCrFeNi}$ HEAs have great potential for structural materials due to their excellent mechanical properties, and their microstructure, phase evolution, and mechanical response have been previously investigated.^{33–35} The irradiation performance, such as precipitation behaviors³¹ and phase stability at high doses,³⁶ has also been reported for coarse-grained $\text{Al}_x\text{CoCrFeNi}$ with varied Al concentrations. However, the radiation behavior of nanostructured $\text{Al}_x\text{CoCrFeNi}$ HEAs is little understood. As nanostructured material design strategy has become a major focus in advanced nuclear material research, the radiation-induced microstructural development such as grain growth of nanostructures^{37–41} is highly relevant to their applications in nuclear reactors. Conventional

Received: October 6, 2020

Revised: January 5, 2021

Published: February 3, 2021



mechanism of grain growth in nanostructured materials was attributed to a thermally assisted, curvature-driven, grain boundary (GB) migration.^{42,43} Few studies were reported on the diffusion-controlled grain growth kinetics^{44,45} and phase stability⁴⁶ in CoCrFeNi and CoCrFeMnNi alloys. However, under radiations, a rapid increase in grain size was observed in nanocrystalline ceria,⁴⁷ zirconia,³⁹ CeO₂,⁴⁰ austenite steel,⁴⁸ and ferrite/martensite steel⁴⁹ at a low temperature, ruling out the thermally activated growth process. However, not all of the grain sizes of nanocrystalline materials increase under irradiation; some have contrary results including TiN/Si bilayers,⁵⁰ Ni,¹⁷ BaS,⁵¹ and 3C-SiC.⁵² The grain growth mechanism of nanocrystalline materials is quite disputed so far. Liu et al.⁵³ stated that the growth rate of Cu thin film is independent of ion flux but associated with the thermal spike diffusion. Based on the direct impact of thermal spikes on grain boundaries, a model to describe grain growth under irradiation in the temperature-independent regime was proposed.²⁰ Molecular dynamics simulations found that ion-induced grain growth was observed when the thermal spike volume is larger than the grain volume or overlaps the grain boundary area.⁵⁴ A faster grain growth was observed under 160 K irradiation as compared to that under 400 K irradiation, meaning grain growth is not thermally activated while being related with the defect-simulated mechanism.³⁹ A study of ceria thin film,⁴⁷ under an irradiation temperature of 160 K, revealed an oxygen vacancy, defect-driven, grain growth mechanism. A study of nanocrystalline oxides⁵⁵ showed a disorder-driven growth process of grain size as a result of the high disorder density near grain boundaries upon ion irradiation. In the present study, nanocrystalline Al_xCoCrFeNi HEAs were irradiated with 1 MeV Kr²⁺ ions to simulate the effect of neutron irradiations, and a significant grain growth was observed with a strong chemical composition dependence. The microstructures and irradiation behaviors of three different Al concentrations were compared and characterized via X-ray diffraction (XRD), transmission electron microscopy (TEM), and energy-dispersive spectroscopy (EDS). In addition, the mechanisms behind the grain growth behaviors of these particular types of alloys were also proposed.

2. EXPERIMENTAL DETAILS

2.1. Material Synthesis and Characterization. Samples with nominal compositions of Al_xCoCrFeNi ($x = 0, 1$, and 2) HEAs were synthesized by high-energy ball milling in an argon gas environment inside a glovebox to protect the powders from oxidation. The pure elements have a purity higher than 99.5% with a particle size smaller than 40 μm . The elements were put into a stainless steel mill pot together with stainless steel balls (8 and 12 mm in diameter and 1:4 in weight percentage, respectively). The weight ratio of the powders to the grinding balls was 1:5, and the large HEA powders were obtained after ball milling for 10 h. Then, 5 more hours of wet ball milling was used to reduce the size of the large HEA powders. Ethanol was applied as the wetting agent. The samples with different Al concentrations ($x = 0, 1, 2$) were denominated to be Al-0, Al-1, and Al-2 alloys. Crystal structures were analyzed using X-ray diffractometer with Cu- $\kappa\alpha$ radiation of wavelength $\lambda = 0.154$ nm and operating at 45 kV and 40 mA. The $\theta-2\theta$ scans in the range of $5-120^\circ$, with a step of 0.02° as well as a scan speed of $5^\circ/\text{min}$, were performed. *Ex situ* TEM observations were made for the microstructures and phases before ion irradiation via a

200 kV JOEL 2011 TEM at a shared instrument facility of Louisiana State University.

2.2. Irradiation Experiments. One MeV Kr²⁺ ion irradiation experiments were conducted at the Intermediate Voltage Electron Microscope (IVEM)-Tandem facility at the Argonne National Laboratory, which has an attached ion accelerator to an electron microscope, operated at 200 kV, so that *in situ* TEM observations of irradiation behaviors of Al_xCoCrFeNi HEAs under intensive ion bombardment can be determined as a function of ion dose. Based on SRIM 2008 calculations, the ion range (~ 300 nm) of 1 MeV Kr would be greater than the thickness of the prepared samples, meaning that the ions would pass through the samples being examined. During ion irradiation, the electron beam was turned off to avoid concurrent electron irradiation damage. The irradiation experiments were performed on TEM samples prepared via the solution-drop method, which powder was dispersed into absolute ethanol using the ultrasonic treatment, and then the solution was deposited onto carbon-coated TEM grids and naturally dried in air. All of the HEA samples were irradiated at room temperature for a comparison of chemical composition dependence on the irradiation performances. The evolution of microstructures was followed by a sequence of bright-field (BF) and dark-field (DF) TEM images as well as selected area electron diffraction (SAED) patterns during irradiation, making the kinetics of irradiation-induced grain growth easier to monitor. DF imaging was obtained by inserting an objective aperture to cover the low-index diffraction rings of the SAED pattern. The threshold displacement energies for the atoms in the Al_xCoCrFeNi HEAs are not available; therefore, a threshold displacement energy of 40 eV was used for SRIM calculation based on other studies.^{31,56} The irradiation fluence can be converted into the ion irradiation doses in the unit of displacements per atom (dpa) using SRIM 2008 software.

3. RESULTS AND DISCUSSION

3.1. Sample Characterization by XRD and TEM. XRD patterns of the as-milled nanocrystalline Al_xCoCrFeNi HEAs are shown in Figure 1. For $x = 0$, all of the diffraction peaks can be identified in a single phase with the face-centered cubic (FCC) crystal structure, suggesting that the pure FCC structure was formed. As the Al concentration increased to $x = 1$, a new structure identified as the body-centered cubic (BCC) crystal structure was observed instead of the FCC

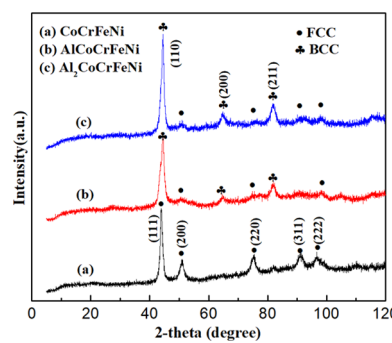


Figure 1. XRD analyses of nanocrystalline Al_xCoCrFeNi high-entropy alloys with various Al contents ($x = 0, 1, 2$), showing the pure FCC crystal structure for CoCrFeNi alloy and primary BCC with the mirror FCC crystal structure for AlCoCrFeNi and Al₂CoCrFeNi alloys.

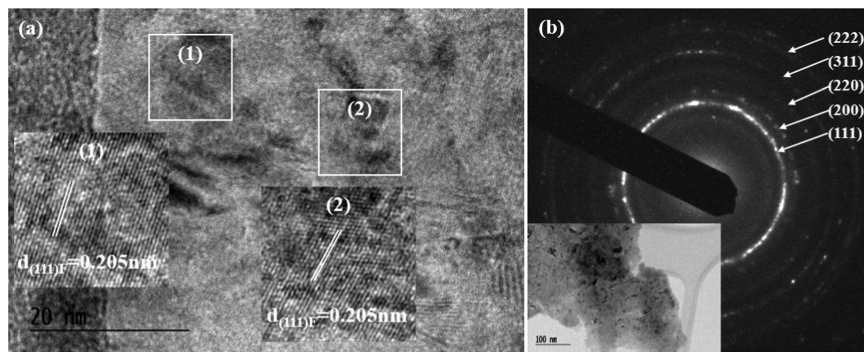


Figure 2. Characterization of the CoCrFeNi high-entropy alloy: (a) high-resolution TEM image showing nanocrystals in a random orientation; the white square indicates the area from which the inset invert FFT images were obtained; and (b) SAED pattern with the pure FCC crystal structure; the corresponding bright-field image was inserted in the left corner.

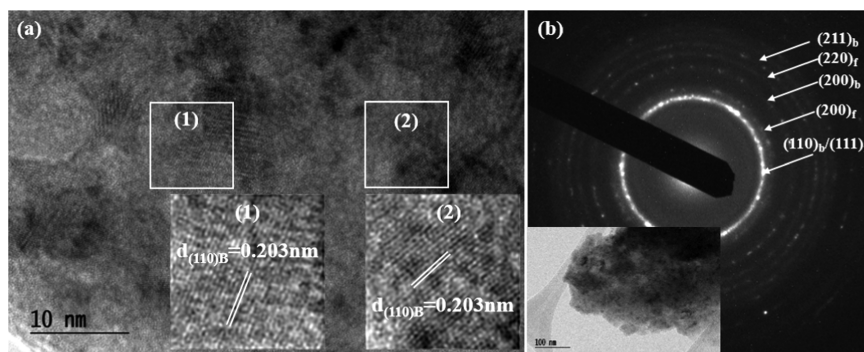


Figure 3. Characterization of the AlCoCrFeNi high-entropy alloy: (a) high-resolution TEM image showing nanocrystals in a random orientation; the white square indicates the area from which the invert FFT images were obtained; and (b) SAED pattern with the BCC + FCC crystal structure; the bright-field image was inserted in the left corner.

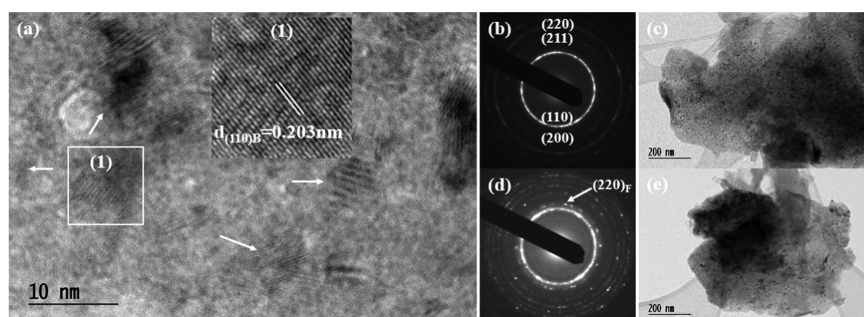


Figure 4. Characterization of the Al₂CoCrFeNi high-entropy alloy: (a) high-resolution TEM image showing nanocrystals in a random orientation; the white square indicates the area from which the invert FFT images were obtained; (b), (c) SAED pattern with the pure BCC crystal structure and the corresponding bright-field image in one area of the sample; and (d), (e) SAED pattern with the combined BCC + FCC crystal structure and the corresponding bright-field image in different areas of the sample.

crystal structure; however, a mirrored phase with the FCC crystal structure corresponding to FCC (200) and (220) can be detected. With the continuous increase in the Al content to $x = 2$, a primary BCC and a mirrored FCC crystal structure can also be observed. The BCC structure is not close-packed compared to the FCC structure, and a phase transformation from the initial FCC to BCC structure can occur to reduce the lattice distortion induced by the atomic size mismatch due to the increase in the Al concentration.⁵⁷

Characterization of nanocrystalline Al_xCoCrFeNi HEAs, via TEM techniques, with different Al concentrations varying from $x = 0$ to 2 is shown in Figures 2–4. A representative high-resolution TEM image of the Al-0 alloy is shown in Figure 2a, and the corresponding invert fast Fourier transform (FFT)

images showing the d -spacing and grain orientation are given in the inset. The SAED pattern with typical polycrystal diffraction rings defined to be the FCC structure is exhibited in Figure 2b with the corresponding BF image inserted in the bottom-left corner. Figure 2a displays the sample with nanostructures in random orientations, and the determination of the SAED pattern showed a single FCC structure, which was in agreement with the XRD result. A representative high-resolution TEM image of the Al-1 alloy is shown in Figure 3a, and the preferable grain orientation of BCC (110) corresponded with the highest peak of the BCC (110) position in the XRD result. The SAED pattern given in Figure 3b showed a combined BCC + FCC crystal structure, further demonstrating the mirrored peaks corresponding to the FCC

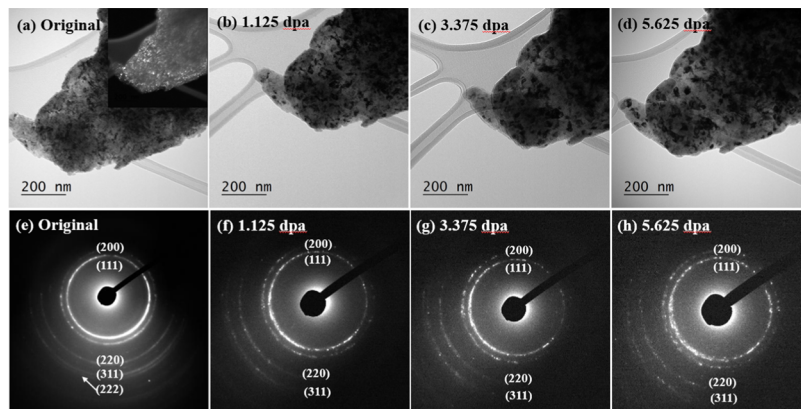


Figure 5. Sequence of bright-field and dark-field TEM images and selected area diffraction patterns taken at different ion doses during irradiation of CoCrFeNi irradiated with 1 MeV Kr²⁺ ions at room temperature, showing ion-irradiation-induced grain growth: (a), (e) original, (b), (f) 1.125 dpa (5.625×10^{14} ion/cm²), (c), (g) 3.375 dpa (1.6875×10^{15} ion/cm²), and (d), (h) 5.625 dpa (2.8125×10^{15} ion/cm²).

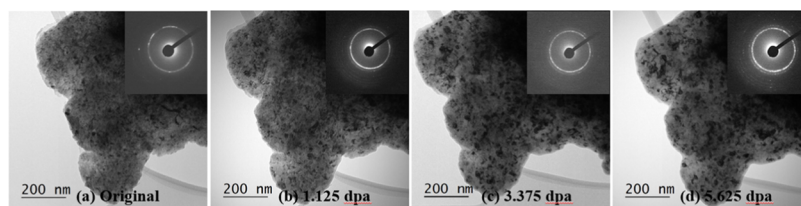


Figure 6. Sequence of bright-field TEM images and selected area diffraction patterns taken at different ion doses during irradiation of AlCoCrFeNi irradiated with 1 MeV Kr²⁺ ions at room temperature, showing ion-irradiation-induced grain growth: (a) original, (b) 1.125 dpa (5.625×10^{14} ion/cm²), (c) 3.375 dpa (1.6875×10^{15} ion/cm²), and (d) 5.625 dpa (2.8125×10^{15} ion/cm²).

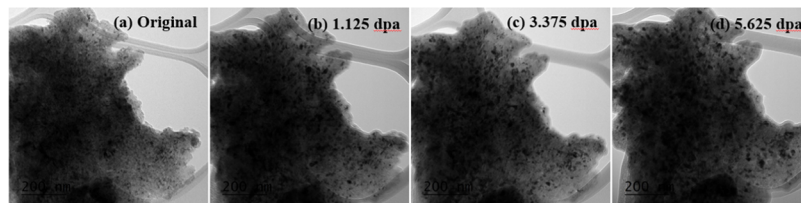


Figure 7. Sequence of bright-field TEM images taken at different ion doses during irradiation of Al₂CoCrFeNi irradiated with 1 MeV Kr²⁺ ions at room temperature, showing ion-irradiation-induced grain growth: (a) original, (b) 1.125 dpa (5.625×10^{14} ion/cm²), (c) 3.375 dpa (1.6875×10^{15} ion/cm²), and (d) 5.625 dpa (2.8125×10^{15} ion/cm²).

structure in the XRD result. The same observation can also be found for the Al-2 alloy, as shown in Figure 4. In different areas of the sample, the single BCC crystal structure and combined BCC + FCC crystal structures were revealed via the SAED technique, as shown in Figure 4b,d, respectively.

3.2. Grain Growth Induced by 1 MeV Kr²⁺ Ions. At room temperature, *in situ* TEM observation revealed a significant ion-irradiation-induced grain growth of nanocrystalline Al_xCoCrFeNi with doses up to 5.625 dpa. A set of TEM BF images and SAED patterns for the Al-0 alloy, as shown in Figure 5, showed a notable grain size increase. Compared to the SAED pattern with complete rings in Figure 5e, which indicated a typical polycrystalline structure, Figure 5f had discrete points, suggesting increased grain size and more aligned orientations. This phenomenon was enhanced by the increase in irradiation dose, indicated by irradiation-induced grain size increase, as shown in Figure 5g,h. Moreover, the growth of nanograins was clearly demonstrated by comparing the contrast of the TEM BF images in Figure 5a–d. The *in situ* TEM observations of the grain growth process for Al-1 and Al-2 alloys are shown in Figures 6 and 7, respectively. By manually measuring the size of more than 35 particles, the average grain

size can be obtained, assuming a spherical geometry from TEM BF images acquired from different regions and averaging them according to the Gaussian distribution. The grain size increased with irradiation dose from 13.8 ± 3 , 7.4 ± 1 , and 11 ± 1 nm before irradiation to 36 ± 8 , 25 ± 5 , and 26.6 ± 3 nm at the irradiation dose of 5.625 dpa for Al-0, Al-1, and Al-2 alloys, respectively. To determine if there was a phase transformation under ion irradiation, a set of SAED patterns were taken and compared with the Al-0 alloy, as shown in Figure 5e,f. The ring index under different irradiation doses was the same and no new diffraction rings were observable due to irradiation, suggesting there was no phase transformation for the Al-0 alloy and the phase stability can be observed under intensive ion irradiation. Nanostructured materials showed a high concentration of grain boundaries (GBs) and interfaces, leading to the different radiation-induced defect behaviors compared with bulk materials due to the limited size in one or more directions. Nanosized materials may be traversed by energetic ions, and the amount of atomic displacement damage in nanostructured materials may be low. Furthermore, a large fraction of GBs and interfaces provide a special environment for defect production, migration, and recombination. There-

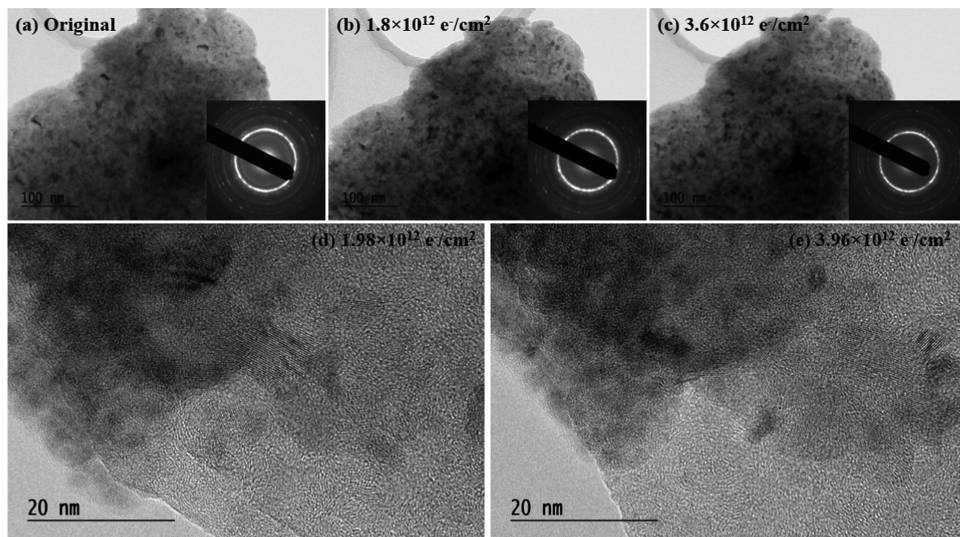


Figure 8. Sequences of bright-field TEM images, selected area diffraction patterns, and high-resolution TEM images taken at different electron doses for AlCoCrFeNi high-entropy alloy irradiated with 200 keV electrons at room temperature, showing no electron-irradiation-induced grain growth: (a) original, (b) 1800 s ($1.8 \times 10^{12} \text{ e}^-/\text{cm}^2$), (c) 3600 s ($3.6 \times 10^{12} \text{ e}^-/\text{cm}^2$), (d) 1800 s ($1.98 \times 10^{12} \text{ e}^-/\text{cm}^2$), and (e) 3600 s ($3.96 \times 10^{12} \text{ e}^-/\text{cm}^2$).

fore, phase stability can be expected as a result of different irradiation damage mechanisms and self-healing behaviors via unique nanostructural evolution in HEAs.

3.3. Grain Growth Kinetics under Ion Irradiation. In the ion–solid interaction, the atomic displacement cascades can create thermal spike with drastically elevated temperatures inside the solid materials. Such transient localized melting under ion irradiation can result in the grain growth in irradiation-affected regions.^{58–60} The driving force was the grain boundary migration and curvature induced by atomic jumps as a result of displacement collision cascade. However, grain growth cannot be induced by the simply isolated displacements but only attributed to the displacement collision cascades that traverse the grain boundary.⁶⁰ This was further confirmed by the result that no grain size increase occurred under a 1 MeV electron irradiation up to 180 dpa for Zr-based thin film, suggesting that only defects created within thermal spikes influence the grain growth kinetics. Under electron irradiation, there may be no cascades and thermal spikes; therefore, no increase in the grain size can be observed. To further demonstrate that grain growth was caused by the thermal spike model in this work, the Al-1 alloy was irradiated with 200 keV electrons at room temperature. Sequences of TEM BF images and SAED patterns, as well as high-resolution TEM images taken at different electron doses, are shown in Figure 8. No growth of the grain size can be observed even after high electron doses by comparing the contrast of the TEM BF images and the diffraction rings in the SAED patterns. The diffraction rings remained to be coherent and no notable discrete points can be observed, and the contrast of the TEM BF images showed no big change after electron irradiation, suggesting that the grain cannot grow under a 200 keV electron irradiation.

Based on this thermal spike model, a power law expression showing the relation between the average grain size and the ion dose was proposed. This expression (listed below) is predicted for the tendency of the grain size increase, where D_0 is the initial average grain size, n is a constant standing for grain growth rate, K is proportional to the GB mobility of the

materials and driving force, and Φ is the ion dose. The grain growth constant n may be the dominating factor affecting growth mechanisms, which may be an intrinsic parameter depending on the material system

$$D^n - D_0^n = K\Phi$$

The fitting parameter n was determined to be 3, 3.5, and 4 for Al-0, Al-1, and Al-2 alloys, based on the coefficient of determination R^2 , and K is determined to be $9028 \pm 663 \text{ nm}^n/\text{dpa}$, $13\,572 \pm 1049 \text{ nm}^n/\text{dpa}$, and $80\,458 \pm 5794 \text{ nm}^n/\text{dpa}$, respectively. Chemical composition dependence on the grain growth has been revealed.⁶⁰ A faster growth of grain size was observed in materials with a lower cohesive energy ΔH_{coh} assuming the atomic jump activation energy scales with the cohesive energy.⁶¹ In the present study, to understand the chemical composition effects on the grain growth kinetics of the $\text{Al}_x\text{CoCrFeNi}$ HEAs, the intrinsic material properties, cohesive energy, were also analyzed. Cohesive energy of an alloy is determined to be a sum of $a \times \Delta H_{\text{coh}}(A) + b \times \Delta H_{\text{coh}}(B)$, where a and b are the atomic fractions of the corresponding components A and B, and $\Delta H_{\text{coh}}(A)$ and $\Delta H_{\text{coh}}(B)$ are the cohesive energies for pure metals A and B, respectively.⁶² The cohesive energies for Al-0, Al-1, and Al-2 alloys were determined to be 4.30, 4.12, and 4.00 eV, respectively.⁶³ It is notable that the grain growth rate n increased from 3.0 to 4.0 with the increase in the concentration of Al from $x = 0$ to 2 as a consequence of the reduction of the cohesive energies. In addition, parameter K also showed a significant variation, which the Al-2 alloy shows a much higher K value than Al-1 and Al-0 alloys, probably indicating a higher grain boundary mobility and driving force for the grain growth process.

It was also noted that, in all grain growth curves, the grain growth rate decreased as the irradiation dose increased such that the grain size saturated at relatively high doses, which may be partly attributed to the loss of driving force with the reduction of the curvature of the GBs. Grain boundary migration is a major driving force for ion-irradiation-induced grain size increase for nanostructured materials under ion

bombardment.⁵⁹ As the grain curvature becomes smaller with increasing grain size, the loss of driving force accounts for the growth of grain size saturation in Figure 9. Moreover, as the

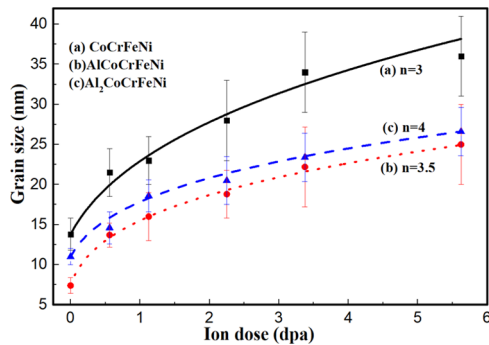


Figure 9. Grain growth stimulated by a 1 MeV Kr²⁺ ion irradiation at 298 K for Al_xCoCrFeNi high-entropy alloys with different Al concentrations ($x = 0, 1, 2$). The grain size variation is within the error bars indicated.

grain size far exceeds the cascade size, the probability of defect cascades occurring near or at the GBs decreases, resulting in the saturation of grain size after a certain ion dose.

Radiation-induced grain growth has been revealed in many materials.^{39,40,49,55} The conventional mechanisms without irradiations were attributed to the thermally assisted grain rotation and curvature-driven mechanisms to reduce the grain boundary curvature. However, we observe grain growth in this work at room temperature, and such low-temperature grain growth does not follow the thermally activated mechanisms. It is worth noting that the grain growth rate decreased rapidly with the increase in the average grain size (as shown in Figure 10). For example, the growth decreased significantly from 11

condition, grain boundaries are likely to migrate and grain size will increase to restore an ordered and equilibrium state of atoms. If the initial grain size is no larger than the damage volume, which is around the order of 10 nm magnitude according to the reference,⁵⁵ the grain growth will occur and reach its minimum rate when the grain size is larger than the ion-irradiation-induced damage volume.⁶⁴ This fast growth mechanism is in good agreement with the present experimental data of the rapid initial grain size increase, and thus, this disorder-driven mechanism is proposed as the dominating growth mechanism for the initial stage of grain growth upon ion irradiation as a result of the very high disorders that spread throughout the grains. In contrast, this disorder mechanism was evaded as the grain grew since a smaller amount of initial disorder cannot induce the movement of grain boundaries for the damaged grains. On the other side, the damaged grains are likely to recover back to their original crystalline order, meaning this disorder-driven mechanism cannot explain the further slower grain growth process. With continuous ion irradiation, a large fraction of point defects (interstitials and vacancies) was induced, and these defects can be accumulated and absorbed by the GBs, which causes a large defect concentration difference near GBs. This defect concentration gradient created a nonequilibrium environment via atomic collision cascades and added the driving force affecting grain growth. Under this nonequilibrium environment, atoms of one grain will be activated to jump across the grain boundary to an available vacant site of the other grain, resulting in the migration of grain boundary and hence the grain growth. Therefore, the further slower grain growth stage was attributed to the defect-simulated mechanism.

4. CONCLUSIONS

Nanocrystalline Al_xCoCrFeNi high-entropy alloys with different Al contents ($x = 0, 1, 2$) were synthesized by high-energy ball milling at room temperature. The crystal structure was determined to be FCC for the Al-0 alloy and BCC + FCC for Al-1 and Al-2 alloys by XRD and TEM techniques. First, a notable grain growth was observed under a 1 MeV Kr²⁺ ion irradiation, which grain size increases with irradiation dose from 13.8 ± 3 , 7.4 ± 1 , and 11 ± 1 nm before irradiation to 36 ± 8 , 25 ± 5 , and 26.6 ± 3 nm at an irradiation dose of 5.625 dpa for Al-0, Al-1, and Al-2 alloys, respectively, and whose kinetics was elucidated by the thermal spike model. On the other hand, radiation-induced grain growth showed a significant chemical composition dependence where the highest grain growth rate was found in the Al-2 alloy as a result of the lowest cohesive energy, which results in the lowest activation energy for atomic jump under ion irradiation. Finally, the initial fast grain growth was attributed to the disorder-driven mechanism, which was caused by the loss of the crystalline order as a result of ion-irradiation-induced large lateral damage volume. The relatively slow grain growth was attributed to the defect-driven mechanism, which the defect concentration difference near GBs was created by the radiation-induced point defects, creating a nonequilibrium environment via atomic collision cascades that is likely to induce the grain boundary migration, leading to the grain size increase.

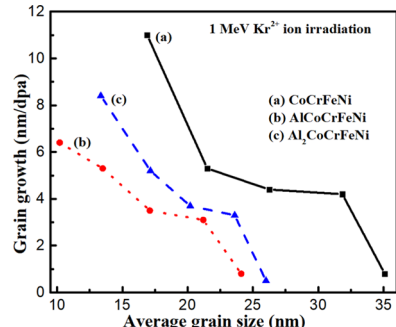


Figure 10. Grain growth with the change in the average grain size, showing the faster grain growth in the smaller grains as compared to the slower grain size increase in the larger grains.

nm/dpa at a grain size of 13.8 nm to 0.8 nm/dpa at a grain size around 35 nm for the Al-0 alloy. The decreased grain growth with the increase in grain size was also observed for Al-1 and Al-2 alloys. A disorder-driven grain growth mechanism was proposed by Aidhy et al.,⁴⁰ in which the growth of the grains can be primarily attributed to the loss of crystalline order due to atomic disorders at or near GBs upon displacive ion irradiation. The atomic and lattice disordering originating from GBs can induce grain growth in nanocrystalline materials since a large lateral damage volume can be caused by ion irradiation. The lateral damage induces a disordered and nonequilibrium state, which most atoms disfavor. Therefore, under this

■ ASSOCIATED CONTENT

SI Supporting Information

The Supporting Information is available free of charge at <https://pubs.acs.org/doi/10.1021/acs.jpcc.0c09061>.

SEM analysis (Figure S1) and EDS analysis (Table S1) of ball-milled powders (large and small particles) of AlCoCrFeNi alloy ([PDF](#))

■ AUTHOR INFORMATION

Corresponding Author

Jianren Zhou – Department of Mechanical and Industrial Engineering, Louisiana State University, Baton Rouge, Louisiana 70803, United States; [ORCID iD](https://orcid.org/0000-0001-7734-2250); Phone: 225-578-7953; Email: jianrenzhou1989@gmail.com; Fax: 225-579-5924

Authors

Md Imdadul Islam – Department of Mechanical and Industrial Engineering, Louisiana State University, Baton Rouge, Louisiana 70803, United States

Shengmin Guo – Department of Mechanical and Industrial Engineering, Louisiana State University, Baton Rouge, Louisiana 70803, United States

Yi Zhang – Department of Mechanical and Industrial Engineering, Louisiana State University, Baton Rouge, Louisiana 70803, United States

Fengyuan Lu – Department of Mechanical and Industrial Engineering, Louisiana State University, Baton Rouge, Louisiana 70803, United States

Complete contact information is available at:
<https://pubs.acs.org/10.1021/acs.jpcc.0c09061>

Notes

The authors declare no competing financial interest.

■ ACKNOWLEDGMENTS

This work was supported by the NRC Faculty Development Grant NRC-38-10-933 and the Louisiana Board of Regents LINK program under contract number NSF(2015)-LINK-97. The authors thank the staff of the IVEM-tandem Facility at the Argonne National Laboratory, Marquis Kirk and Peter Baldo, for assistance in ion irradiation experiments and in situ TEM observation. The data that support the findings of this study are available from the corresponding author [J.Z.] upon request.

■ REFERENCES

- (1) Cantor, B.; Chang, I.; Knight, P.; Vincent, A. Microstructural development in equiatomic multicomponent alloys. *Mater. Sci. Eng. A* **2004**, *375–377*, 213–218.
- (2) Hsu, C.-Y.; Yeh, J.-W.; Chen, S.-K.; Shun, T.-T. Wear resistance and high-temperature compression strength of Fcc CuCoNiCrAl0.5Fe alloy with boron addition. *Metall. Mater. Trans. A* **2004**, *35*, 1465–1469.
- (3) Otto, F.; Dlouhý, A.; Somsen, C.; Bei, H.; Eggeler, G.; George, E. P. The influences of temperature and microstructure on the tensile properties of a CoCrFeMnNi high-entropy alloy. *Acta Mater.* **2013**, *61*, 5743–5755.
- (4) Gali, A.; George, E. P. Tensile properties of high-and medium-entropy alloys. *Intermetallics* **2013**, *39*, 74–78.
- (5) Gludovatz, B.; Hohenwarter, A.; Catoor, D.; Chang, E. H.; George, E. P.; Ritchie, R. O. A fracture-resistant high-entropy alloy for cryogenic applications. *Science* **2014**, *345*, 1153–1158.

(6) Tong, C.-J.; Chen, M.-R.; Yeh, J.-W.; Lin, S.-J.; Chen, S.-K.; Shun, T.-T.; Chang, S.-Y. Mechanical performance of the Al x CoCrCuFeNi high-entropy alloy system with multiprincipal elements. *Metall. Mater. Trans. A* **2005**, *36*, 1263–1271.

(7) Wu, J.-M.; Lin, S.-J.; Yeh, J.-W.; Chen, S.-K.; Huang, Y.-S.; Chen, H.-C. Adhesive wear behavior of Al x CoCrCuFeNi high-entropy alloys as a function of aluminum content. *Wear* **2006**, *261*, 513–519.

(8) Chen, Y.; Duval, T.; Hung, U.; Yeh, J.; Shih, H. Microstructure and electrochemical properties of high entropy alloys—a comparison with type-304 stainless steel. *Corros. Sci.* **2005**, *47*, 2257–2279.

(9) Hsu, Y.-J.; Chiang, W.-C.; Wu, J.-K. Corrosion behavior of FeCoNiCrCu x high-entropy alloys in 3.5% sodium chloride solution. *Mater. Chem. Phys.* **2005**, *92*, 112–117.

(10) Greer, A. L. Confusion by design. *Nature* **1993**, *366*, 303–304.

(11) Islam, M. I. *Effect of Elevated Temperature and Pulse Laser on Surface Morphology, Fracture, and Fatigue Behavior of Selective Materials for Nuclear Structural Applications*; MS, Tuskegee University: Tuskegee, AL, 2016.

(12) Yvon, P.; Carré, F. Structural materials challenges for advanced reactor systems. *J. Nucl. Mater.* **2009**, *385*, 217–222.

(13) Zinkle, S. J.; Was, G. Materials challenges in nuclear energy. *Acta Mater.* **2013**, *61*, 735–758.

(14) Islam, M. I.; Moon, F.; Aglan, H. *Effect of Extreme Environmental Temperature on the Fracture Resistance, and Fatigue Behavior of Dual Phase Ti-6Al-4V Alloy*, ASTFE Digital Library; Begel House Inc., 2020.

(15) Was, G.; Pettit, D.; Ukai, S.; Zinkle, S. Materials for future nuclear energy systems. *J. Nucl. Mater.* **2019**, *527*, No. 151837.

(16) Islam, M.; Fermin, C.; Aglan, H. Microscopic Origin of Strength and Microhardness of Titanium Alloy at Elevated Temperature. *Microsc. Microanal.* **2015**, *21*, 287–288.

(17) Nita, N.; Schaeublin, R.; Victoria, M. Impact of irradiation on the microstructure of nanocrystalline materials. *J. Nucl. Mater.* **2004**, *329*, 953–957.

(18) Islam, M.; Moon, F.; Aglan, H. *Influence of Heat Treatment on Mechanical Properties, Microstructure, and Fracture Surface Morphology of V-5Cr-5Ti Alloy*, ASTFE Digital Library; Begel House Inc., 2020.

(19) Xia, S.; Yang, X.; Yang, T.; Liu, S.; Zhang, Y. Irradiation resistance in Al x CoCrFeNi high entropy alloys. *JOM* **2015**, *67*, 2340–2344.

(20) Kaoumi, D.; Motta, A. T.; Birtcher, R. A thermal spike model of grain growth under irradiation. *J. Appl. Phys.* **2008**, *104*, No. 073525.

(21) Islam, M. I.; Lu, F. *Mechanical Properties of Thermally Stable Cadmium Iodoapatite Ceramic by Reactive Spark Plasma Sintering Technique*, ASTFE Digital Library; Begel House Inc., 2020.

(22) Senkov, O. N.; Wilks, G.; Scott, J.; Miracle, D. B. Mechanical properties of Nb25Mo25Ta25W25 and V20Nb20Mo20Ta20W20 refractory high entropy alloys. *Intermetallics* **2011**, *19*, 698–706.

(23) Zhang, Y.; Liu, Y.; Li, Y.; Chen, X.; Zhang, H. Microstructure and mechanical properties of a refractory HfNbTiVSi0.5 high-entropy alloy composite. *Mater. Lett.* **2016**, *174*, 82–85.

(24) Senkov, O.; Woodward, C. Microstructure and properties of a refractory NbCrMo0.5Ta0.5TiZr alloy. *J. Mater. Sci. Eng. A* **2011**, *S29*, 311–320.

(25) Senkov, O.; Wilks, G.; Miracle, D.; Chuang, C.; Liaw, P. Refractory high-entropy alloys. *Intermetallics* **2010**, *18*, 1758–1765.

(26) Ettefagh, A. H.; Wen, H.; Chaichi, A.; Islam, M. I.; Lu, F.; Gartia, M.; Guo, S. Laser surface modifications of Fe-14Cr ferritic alloy for improved corrosion performance. *Surf. Coat. Technol.* **2020**, *381*, No. 125194.

(27) Yao, H.; Katona, R.; Zhou, J.; Islam, M. I.; Raush, J.; Lu, F.; Guo, S. In *Defects Evaluation of Selective Laser Melting Stainless Steel 316 Parts Using Positron Annihilation Lifetime Measurement*, ASME 2018 International Mechanical Engineering Congress and Exposition, 2018.

(28) Nagase, T.; Anada, S.; Rack, P. D.; Noh, J. H.; Yasuda, H.; Mori, H.; Egami, T. Electron-irradiation-induced structural change in Zr–Hf–Nb alloy. *Intermetallics* **2012**, *26*, 122–130.

- (29) Nagase, T.; Anada, S.; Rack, P. D.; Noh, J. H.; Yasuda, H.; Mori, H.; Egami, T. MeV electron-irradiation-induced structural change in the bcc phase of Zr–Hf–Nb alloy with an approximately equiatomic ratio. *Intermetallics* **2013**, *38*, 70–79.
- (30) Nagase, T.; Rack, P. D.; Noh, J. H.; Egami, T. In-situ TEM observation of structural changes in nano-crystalline CoCrCuFeNi multicomponent high-entropy alloy (HEA) under fast electron irradiation by high voltage electron microscopy (HVEM). *Intermetallics* **2015**, *59*, 32–42.
- (31) Yang, T.; Xia, S.; Liu, S.; Wang, C.; Liu, S.; Fang, Y.; Zhang, Y.; Xue, J.; Yan, S.; Wang, Y. Precipitation behavior of $\text{Al}_x\text{CoCrFeNi}$ high entropy alloys under ion irradiation. *Sci. Rep.* **2016**, *6*, No. 32146.
- (32) Kumar, N. K.; Li, C.; Leonard, K.; Bei, H.; Zinkle, S. Microstructural stability and mechanical behavior of FeNiMnCr high entropy alloy under ion irradiation. *Acta Mater.* **2016**, *113*, 230–244.
- (33) Yang, T.; Xia, S.; Liu, S.; Wang, C.; Liu, S.; Zhang, Y.; Xue, J.; Yan, S.; Wang, Y. Effects of Al addition on microstructure and mechanical properties of $\text{Al}_x\text{CoCrFeNi}$ high-entropy alloy. *J. Mater. Sci. Eng., A* **2015**, *648*, 15–22.
- (34) Wang, W.-R.; Wang, W.-L.; Wang, S.-C.; Tsai, Y.-C.; Lai, C.-H.; Yeh, J.-W. Effects of Al addition on the microstructure and mechanical property of $\text{Al}_x\text{CoCrFeNi}$ high-entropy alloys. *Intermetallics* **2012**, *26*, 44–51.
- (35) Tang, Z.; Gao, M. C.; Diao, H.; Yang, T.; Liu, J.; Zuo, T.; Zhang, Y.; Lu, Z.; Cheng, Y.; Zhang, Y. Aluminum alloying effects on lattice types, microstructures, and mechanical behavior of high-entropy alloys systems. *JOM* **2013**, *65*, 1848–1858.
- (36) Xia, S.; Gao, M. C.; Yang, T.; Liaw, P. K.; Zhang, Y. Phase stability and microstructures of high entropy alloys ion irradiated to high doses. *J. Nucl. Mater.* **2016**, *480*, 100–108.
- (37) Lian, J.; Zhang, J.; Namavar, F.; Zhang, Y.; Lu, F.; Haider, H.; Garvin, K.; Weber, W. J.; Ewing, R. C. Ion beam-induced amorphous-to-tetragonal phase transformation and grain growth of nanocrystalline zirconia. *Nanotechnology* **2009**, *20*, No. 245303.
- (38) Zhang, Y.; Edmondson, P. D.; Varga, T.; Moll, S.; Namavar, F.; Lan, C.; Weber, W. J. Structural modification of nanocrystalline ceria by ion beams. *Phys. Chem. Chem. Phys.* **2011**, *13*, 11946–11950.
- (39) Zhang, Y.; Jiang, W.; Wang, C.; Namavar, F.; Edmondson, P. D.; Zhu, Z.; Gao, F.; Lian, J.; Weber, W. J. Grain growth and phase stability of nanocrystalline cubic zirconia under ion irradiation. *Phys. Rev. B* **2010**, *82*, No. 184105.
- (40) Aidhy, D. S.; Zhang, Y.; Weber, W. J. A fast grain-growth mechanism revealed in nanocrystalline ceramic oxides. *Scr. Mater.* **2014**, *83*, 9–12.
- (41) Kaoumi, D.; Motta, A.; Birtcher, R. Grain growth in nanocrystalline metal thin films under in situ ion-beam irradiation. *J. ASTM Int.* **2007**, *8*, 1–13.
- (42) Haslam, A.; Phillipot, S.; Wolf, D.; Moldovan, D.; Gleiter, H. Mechanisms of grain growth in nanocrystalline fcc metals by molecular-dynamics simulation. *Mater. Sci. Eng., A* **2001**, *318*, 293–312.
- (43) Moore, L. J.; Dear, R. D.; Summers, M. D.; Dullens, R. P.; Ritchie, G. A. Direct observation of grain rotation-induced grain coalescence in two-dimensional colloidal crystals. *Nano Lett.* **2010**, *10*, 4266–4272.
- (44) Praveen, S.; Basu, J.; Kashyap, S.; Kottada, R. S. Exceptional resistance to grain growth in nanocrystalline CoCrFeNi high entropy alloy at high homologous temperatures. *J. Alloys Compd.* **2016**, *662*, 361–367.
- (45) Vaidya, M.; Anupam, A.; Bharadwaj, J. V.; Srivastava, C.; Murty, B. Grain growth kinetics in CoCrFeNi and CoCrFeMnNi high entropy alloys processed by spark plasma sintering. *J. Alloys Compd.* **2019**, *791*, 1114–1121.
- (46) Vaidya, M.; Karati, A.; Marshal, A.; Pradeep, K.; Murty, B. Phase evolution and stability of nanocrystalline CoCrFeNi and CoCrFeMnNi high entropy alloys. *J. Alloys Compd.* **2019**, *770*, 1004–1015.
- (47) Edmondson, P.; Zhang, Y.; Moll, S.; Namavar, F.; Weber, W. J. Irradiation effects on microstructure change in nanocrystalline ceria—Phase, lattice stress, grain size and boundaries. *Acta Mater.* **2012**, *60*, 5408–5416.
- (48) Radiguet, B.; Etienne, A.; Pareige, P.; Sauvage, X.; Valiev, R. Irradiation behavior of nanostructured 316 austenitic stainless steel. *J. Mater. Sci.* **2008**, *43*, 7338–7343.
- (49) Liu, W.; Zhang, C.; Ji, Y.; Yang, Z.; Zang, H.; Shen, T.; Chen, L. Irradiation-induced grain growth in nanocrystalline reduced activation ferrite/martensite steel. *Appl. Phys. Lett.* **2014**, *105*, No. 121905.
- (50) Popović, M.; Novaković, M.; Šiljegović, M.; Bibić, N. Effects of 200 keV argon ions irradiation on microstructural properties of titanium nitride films. *Nucl. Instrum. Methods Phys. Res., Sect. B* **2012**, *279*, 144–146.
- (51) Singh, S.; Kumar, R.; Singh, N. Effect of swift heavy ion irradiation on bismuth doped BaS nanostructures. *J. Alloys Compd.* **2011**, *509*, L81–L84.
- (52) Jiang, W.; Wang, H.; Kim, I.; Zhang, Y.; Weber, W. J. Amorphization of nanocrystalline 3C–SiC irradiated with Si+ ions. *J. Mater. Res.* **2010**, *25*, 2341–2348.
- (53) Liu, J. C.; Li, J.; Mayer, J. Temperature effect on ion-irradiation-induced grain growth in Cu thin films. *J. Appl. Phys.* **1990**, *67*, 2354–2358.
- (54) Voegeli, W.; Albe, K.; Hahn, H. Simulation of grain growth in nanocrystalline nickel induced by ion irradiation. *Nucl. Instrum. Methods Phys. Res., Sect. B* **2003**, *202*, 230–235.
- (55) Zhang, Y.; Aidhy, D. S.; Varga, T.; Moll, S.; Edmondson, P. D.; Namavar, F.; Jin, K.; Ostrouchov, C. N.; Weber, W. J. The effect of electronic energy loss on irradiation-induced grain growth in nanocrystalline oxides. *Phys. Chem. Chem. Phys.* **2014**, *16*, 8051–8059.
- (56) Xia, S.; Yang, X.; Yang, T.; Liu, S.; Zhang, Y. Irradiation resistance in $\text{Al}_x\text{CoCrFeNi}$ high entropy alloys. *JOM* **2015**, *67*, 2340–2344.
- (57) Zhou, Y.; Zhang, Y.; Wang, F.; Chen, G. Phase transformation induced by lattice distortion in multiprincipal component Co Cr Fe Ni $\text{Cu}_x \text{Al}_{1-x}$ solid-solution alloys. *Appl. Phys. Lett.* **2008**, *92*, No. 241917.
- (58) Liu, J. C.; Li, J.; Mayer, J. Temperature effect on ion-irradiation-induced grain growth in Cu thin films. *J. Appl. Phys.* **1990**, *67*, 2354–2358.
- (59) Kaoumi, D.; Motta, A.; Birtcher, R. Grain growth in Zr–Fe thin films during in situ ion irradiation in a TEM. *Nucl. Instrum. Methods Phys. Res., Sect. B* **2006**, *242*, 490–493.
- (60) Kaoumi, D.; Motta, A.; Birtcher, R. A thermal spike model of grain growth under irradiation. *J. Appl. Phys.* **2008**, *104*, No. 073525.
- (61) Johnson, W.; Cheng, Y.; Van Rossum, M.; Nicolet, M. When is thermodynamics relevant to ion-induced atomic rearrangements in metals? *Nucl. Instrum. Methods Phys. Res., Sect. B* **1985**, *7*, 657–665.
- (62) Liu, J. C. *Ion-Irradiation-Induced Grain Growth and Lateral Thin-Film Reactions*; Cornell University: Ithaca, NY, 1989.
- (63) Kittel, C.; Paul, M. *Introduction to Solid State Physics*; Wiley: New York, 1996; Vol. 8, pp 105–130.
- (64) Liu, J. C.; Nastasi, M.; Mayer, J. Ion irradiation induced grain growth in Pd polycrystalline thin films. *J. Appl. Phys.* **1987**, *62*, 423–428.